Chemical Science

ROYAL SOCIETY OF CHEMISTRY

EDGE ARTICLE

View Article Online
View Journal | View Issue

Cite this: *Chem. Sci.*, 2023, **14**, 3630

All publication charges for this article have been paid for by the Royal Society of Chemistry

Received 19th August 2022
Accepted 24th February 2023

DOI: 10.1039/d2sc04636a

rsc.li/chemical-science

Photo-induced defluorination acyl fluoride exchange as a fluorogenic photo-click reaction for photo-affinity labeling†

Lijun Deng, Cefei Zhang, Baolin Li, Jielin Fu, Zhong Zhang, Sitong Li, Xiaohu Zhao, Zhishan Su, Changwei Hu * and Zhipeng Yu *

Photo-click chemistry has emerged as a powerful tool for revolutionizing bioconjugation technologies in pharmacological and various biomimetic applications. However, enriching the photo-click reactions to expand the bioconjugation toolkit remains challenging, especially when focusing on spatiotemporal control endowed by light activation. Herein, we describe a photo-induced defluorination acyl fluoride exchange (photo-DAFEx) as a novel type of photo-click reaction that is mediated through acyl fluorides produced by the photo-defluorination of *m*-trifluoromethylaniline to covalently conjugate with primary/secondary amines and thiols in an aqueous environment. (TD)-DFT calculations, together with experimental discovery, indicate that the *m*-$NH_2PhF_2C(sp^3)$–F bond in the excited triplet state is cleaved by water molecules, which is key to inducing defluorination. Intriguingly, the benzoyl amide linkages built by this photo-click reaction exhibited a satisfactory fluorogenic performance, which allowed visualization of its formation *in situ*. Accordingly, this photo-controlled covalent strategy was exploited not only for the decoration of small molecules, peptide cyclization and functionalization of proteins *in vitro*, but also for designing photo-affinity probes targeting endogenous carbonic anhydrase II (hCA-II) in living cells.

Introduction

Click chemistry has become an essential strategy for bioconjugation, benefiting from characteristics such as accessibility, smart operation and reliable efficiency. Over the past decade, sulfur(VI) fluoride exchange (SuFEx) has served as an emerging click strategy and has been employed in protein engineering and drug discovery, as it enables crosslinking toward natural nucleophilic residues with excellent specificity (Scheme 1a).[1–3] Therefore, ligand-directed covalent-linking strategies are flourishing by designing probes harbouring the above features, emphasizing the site-dependent reactivity of SuFEx in combination with the target affinity of the ligands.[4] Moreover, the small size of sulfur(VI) fluoride and its high resistance to hydrolysis also allows its easy incorporation into biomacromolecules for profiling of protein-related interactions in a complex biological environment.[4b]

Although thermodynamic ligation approaches, including SuFEx, have enabled numerous pharmacological explorations, some inherent intractable issues are still unsolved, *e.g.*, off-target reactivity at high dosage, off-site launching induced by the microenvironment during delivery,[5] and inability to be applied to single cells.[6] Light-triggered click chemistry provides alternative pathways to build covalent linkages *via* non-invasive manipulation.[7] Scientists have successfully harnessed photo-

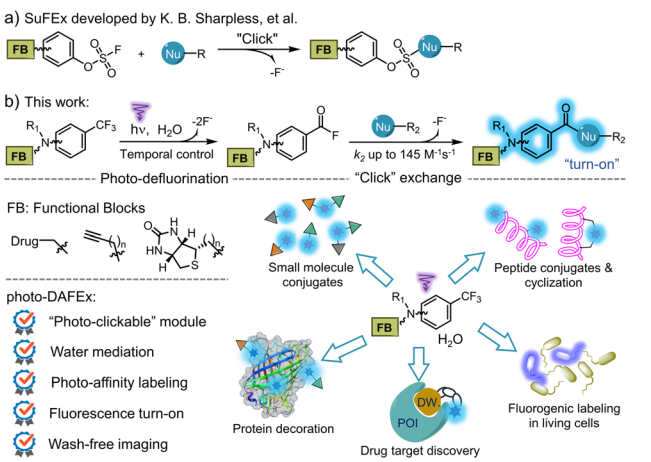

Scheme 1 Illustration of the SuFEx and the photo-DAFEx reactions for fluorogenic functionalization of small molecules and native biomolecules.

Key Laboratory of Green Chemistry & Technology of Ministry of Education, College of Chemistry, Sichuan University, 29 Wangjiang Road, Chengdu 610064, P. R. China. E-mail: changweihu@scu.edu.cn; zhipengy@scu.edu.cn

† Electronic supplementary information (ESI) available: Containing details on experimental procedures, spectra property, and characterization of all new compounds. See DOI: https://doi.org/10.1039/d2sc04636a

stimulation to initiate click reactions *via* the *in situ* generation of intermediates with high reactivity and selectivity, allowing conjugation with spatiotemporal controllability.[8]

Most of the available photo-clickable reagents find an appropriate partner-group after photo-activation, according to their respective characteristics in various bioorthogonal scenarios. Current achievements include photo-released cycloalkyne clicking with azide;[9] tetrazole or sydnone photo-cycloaddition with alkene/-yne;[10,11] photo-promoted hetero-Diels–Alder (HDA)[12] and IEDDA reactions;[13] light-activated thiol-ene/-yne conjugations;[14,15] and light-triggered phenanthrenequinone–alkene HDA reactions.[16] In these scenarios, a biocompatible handle has to be incorporated into the biomacromolecules oriented on specific sites prior to photoligation.

Light-triggered bioconjugation approaches also show exciting promise in both affinity-based probing[17] and protein–protein interactions,[18] which target canonical residues on the active site of proteins. Conventionally, diazirines, aryl azides and benzophenones are widely used photo-crosslinkers for biomedical discovery, displaying high insertion reactivity but diverse chemo-targets.[19] Recently, diazocoumarins,[20] *N*-phenyltetrazole,[21] acyl silanes[22] and *o*-nitrobenzyl alcohols[23] have appeared as novel photo-crosslinkers. In addition to their photo-controllability, these strategies play an important role in advancing the fluorogenic performance with tuneable chemo-specificity. However, the photon-energy utilization efficiency as well as the lifetime of photo-generated intermediate[24] are the two key factors that have to be considered to achieve a photo-crosslinking method with high controllability. The prerequisites for a robust photo-crosslinking reaction also encompass biostability and compact size of the photoactivatable precursor. Furthermore, the covalent-bond formation promoted by the proximity of the photo-generated active moiety tagged on the client molecules[3] is dictated by the microenvironment in which the precursor is incorporated. Given these demands, developing a photo-click reaction that satisfies all of the features in a single solution remains challenging, but desirable.

We recognized that *m*-trifluoromethylaniline derivatives could be activated by light to condensate into amide oligomers based on photo-defluorination.[25] After careful optimization of this photochemical process, a photo-induced defluorination acyl fluorides exchange (photo-DAFEx, Scheme 1b) was discovered as a novel class of photo-click reactions for covalent conjugation towards primary/secondary amines and thiols. Distinct from conventional photo-defluorination, we found

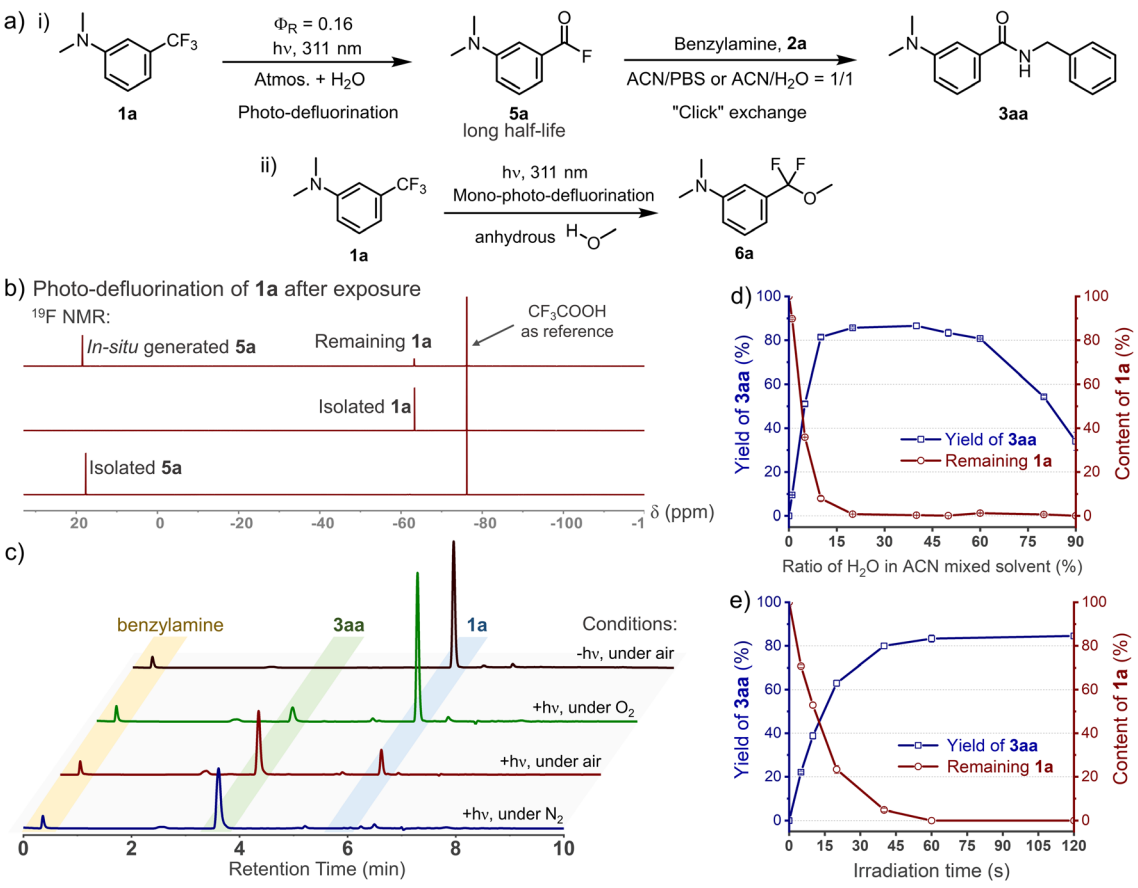

Fig. 1 Experimental studies on the mechanism of the photo-DAFEx. (a) General scheme for the photo-click reaction of **1a** in either (i) aqueous buffer with **2a** or (ii) in absolute methanol. (b) ^{19}F-NMR spectra for identifying *in situ* generated **5a** from **1a** (0.12 mmol) in ACN/H_2O = 1/1 after 30 min irradiation. (c) HPLC traces for the quenching tests of the excited triplet state under various conditions. Screening for the photo-DAFEx conditions of **1a** (100 μM): (d) the ratio of water in the ACN mixture; (e) temporal control by the irradiation time (311 nm, 5.9 mW cm^{-2}).

that water molecules were indispensable for polarizing the C(sp^3)-F bond in *m*-trifluoromethylaniline in the excited triplet state, which resulted in consecutive hydrolytic C–F bond cleavages to yield acyl fluorides (Scheme 1b) in an aqueous environment. The *in situ* generated acyl fluorides with satisfactory stability and muted polarity are capable of exchanging with the primary/secondary amines and thiols to establish benzamide linkages toward small molecules, peptides and proteins, accompanied by a fluorescence turn-on feature (Scheme 1b). To demonstrate potential benefits in chemoproteomic and pharmacological research, the *m*-trifluoromethylaniline motif has been embedded into sulfonamide inhibitors for photo-affinity labeling of endogenous hCA-II in human embryonic kidney cells (HEK-293T). Given the accessibility of *m*-trifluoromethylaniline derivatives, the photo-DAFEx reaction not only enriches the toolbox of photo-click chemistry, but also integrates the photo-labeling and the fluorescence tracking features into a single photo-chemical cascade.

Results and discussion

Design and optimization of the photo-DAFEx reaction

C(sp^3)–F bond cleavage strategies have been realized widely in organic phases, while few reports discuss water-mediated and catalyst-free photo-defluorination strategies that are amenable to biochemical studies.[26] Inspired by the photolysis of flufenamic acid,[25] we found that *N*,*N*-dimethyl-3-(trifluoromethyl) aniline (**1a**) could be efficiently converted to 3-(dimethylamino)benzoyl fluoride (**5a**) after exposure to 311 nm irradiation in an ACN/H_2O mixed solvent (v/v = 1/1) (Fig. 1a). However, *ortho*-/*para*-trifluoromethylaniline showed relatively low efficiency in photo-conversion (Fig. S1, ESI†). Due to the electrostatic stability of the PhCO–F bond, benzoyl fluorides show resistance to hydrolysis (half-life, $t_{1/2}$ = 13.7 h, 298 K, Fig. S6, ESI†), which is akin to the sulfonyl fluorides in SuFEx.[27] Thereby, its isolation after the photo-defluorination in aqueous medium was successful without strong nucleophiles (Fig. 1b). *In situ* photo-generated **5a** could be further amidated with benzylamine (**2a**), furnishing *N*-benzyl-3-(dimethylamino)benzamide (**3aa**) quantitatively.

Oxygen is an efficient quencher of excited triplet states; hence, nitrogen protection is often essential in many photocatalytic reactions.[28] Indeed, suppression is observed in terms of the photo-conversion of **1a** in the photo-DAFEx under air *vs.* under a nitrogen atmosphere (Fig. 1c). In particular, the photochemical conversion can be halted *via* oxygen saturation. However, free radical quenching by TEMPO, styrene, *etc.*, has little influence on the photo-DAFEx (Fig. S2, ESI†). Therefore, the photo-defluorination of **1a** likely occurs in an excited triplet state rather than a radical process. Unexpectedly, water molecules appear to be involved in the photo-defluorination, because the photo-conversion of **1a** is negligible in an anhydrous condition (Fig. 1d). Next, we evaluated the photon utilization efficiency of the photo-DAFEx, in which the quantum yield (Φ_R) was determined to be 0.17 for **1a** under 311 nm irradiation (for **1a** derivatives, see Table S1, ESI†). Within 60 s of irradiation, the conversion of 100 μM **1a** reached completion, affording **3aa** with 86% yield, indicating the high efficiency of the photo-DAFEx (Fig. 1e). To assess the biostability of *m*-trifluoromethylanilines, 100 μM **1a** or **1e** was treated with a 50-fold excess concentration of glutathione (5.0 mM GSH) in ACN/PBS solution (v/v = 1/1, pH = 7.4, 298 K). 71% of **1a** and 97% of **1e** remained after incubation for 72 h (Fig. S4, ESI†), suggesting excellent resistance to nucleophilic additions in a biomimicking environment in the dark. Optimization of the photo-reaction conditions, including the pH of the aqueous buffer and organic cosolvents (Table S2, ESI†), indicated that physiological conditions (PBS, pH = 7.4) are favourable in terms of the yield of **3aa** (94%), while the use of an organic cosolvent brings about trivial variation in the yield, except in the case of methanol. Accordingly, absolute methanol, which acts as a protic solvent, was adopted in the photo-DAFEx, which resulted in the detection of 3-(dimethylamino) difluorobenzyl methyl ether (**6a**, Fig. 1a and S5, ESI†) with up to 17% HPLC yield. The successful capture of the mono-defluorination product (**6a**) clarified that the photo-induced dual defluorination is a stepwise process. This series of experimental phenomena aroused our interest in studying the mechanism of the photo-DAFEx reaction.

DFT calculation of the photo-DAFEx mechanism in an aqueous environment

DFT calculations at the M06-2X(D3)/6-31+G** theoretical level (all Gibbs free energies below were calculated using Shermo 2.3,[29] and the wavefunction analyses were performed using Multiwfn 3.8,[30] for more details, see ESI computational details†) were performed to understand the mechanism of the photo-defluorination of **1a** (Fig. 2a). As a comparison, a thermodynamic defluorination gives 3-(dimethylamino)difluorobenzyl alcohol (**IM3**) with an activation free energy barrier ($\Delta G^{\ddagger}$) of as high as 49.4 kcal mol^{-1}, which is quite harsh for a biocompatible ligation. Unlike the ground-state process, the first photo-defluorination step in the excited triplet state was found to involve a unique fluorine–oxygen swap mode, and thereby has to be subdivided: (i) the first C(sp^3)–F bond breakage (**TS3-T_1**) is evoked by hydrogen-bonding-assisted polarization in harmony with triplet-state charge delocalization to form a stabilized ionic complex (**IM5-T_1**). (ii) Then, the $C2^+$ atom in **IM5-T_1** is attacked by the adjacent oxygen atom in the water molecule with a negative charge acquired from $F1^-$ (**TS4-T_1**) in the counter ion, affording **IM6-T_1**. The activation barriers *via* **TS3-T_1** (4.8 kcal mol^{-1}) and **TS4-T_1** (14.7 kcal mol^{-1}) are significantly lower than that in the ground state ($\Delta G^{\ddagger}$ = 49.4 kcal mol^{-1}). As a result, the first C(sp^3)–F bond cleavage proceeds instantly in the excited triplet state *via* light activation. Subsequent non-radiative quenching of **IM6-T_1** to **IM2** is computed to be thermodynamically favoured (ΔG = −69.1 kcal mol^{-1}). Due to the instability of **IM3** in an aqueous environment, the benzoyl fluoride (**5a**) is obtained through a fluorine atom elimination *via* a six-membered cyclic transition state (**TS2**) with a dual H-bonding activation by water molecules in the ground state ($\Delta G^{\ddagger}$ = 20.5 kcal mol^{-1}). As evidence for this pathway, **6a**

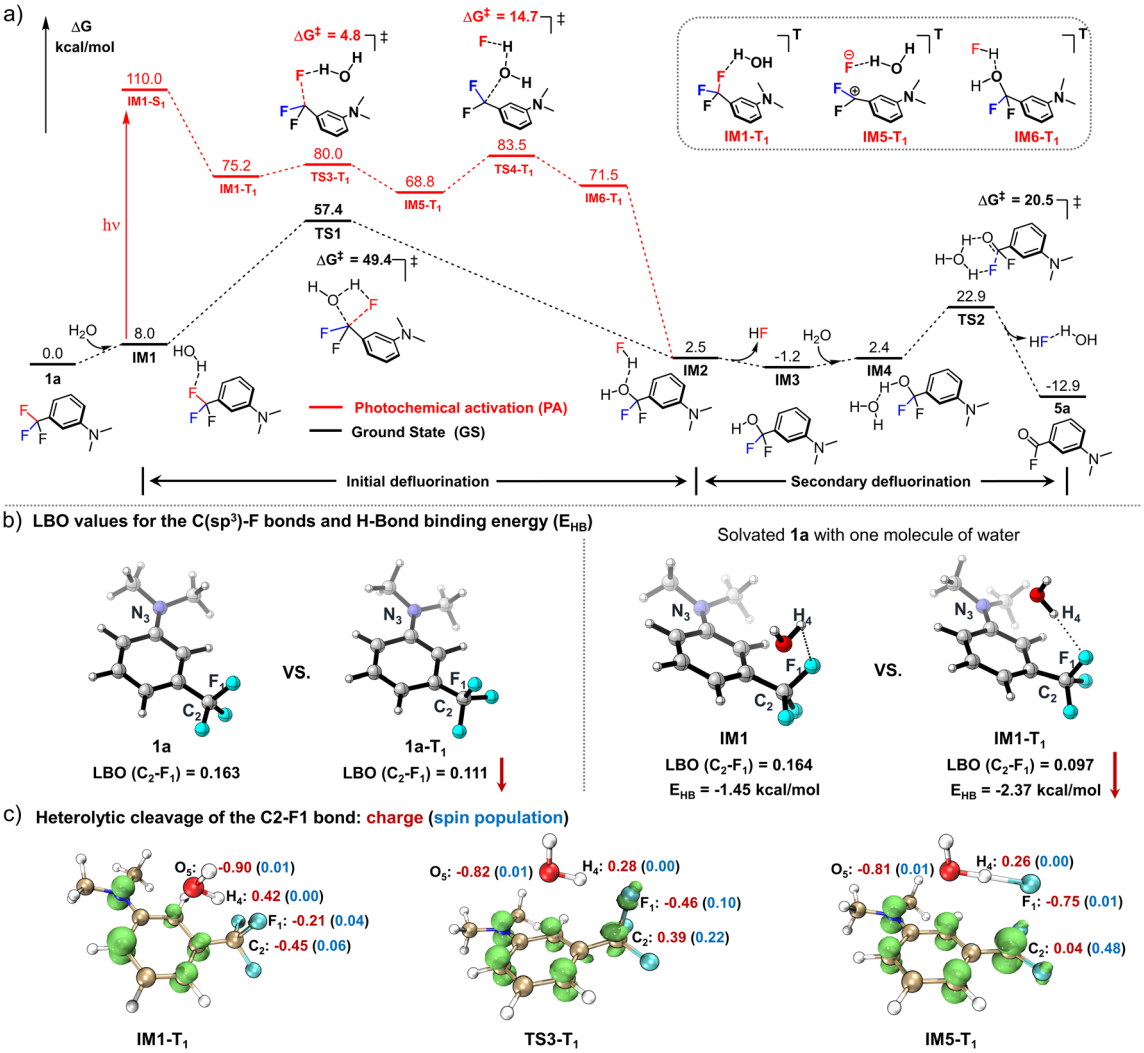

Fig. 2 Computational studies for deciphering the mechanism of the photo-DAFEx reaction. (a) Gibbs energy profile for the defluorination process of **1a** to afford the intermediate **5a**; the black-colour pathway is the thermodynamic path in the ground state (GS), while the red-colour pathway is followed in the first excited triplet state (T_1); free energies were calculated at the M06-2X(D3)/ma-TZVP level (Table S8, ESI†). (b) LBO value of the key C–F bond in the denoted structures (**1a** *vs.* **1a-T$_1$**, **IM1** *vs.* **IM1-T$_1$**), and the hydrogen bond strength (E_{HB}) between the HO–H and the F_1 atoms computed with ρ_{BCP}. (c) Spin density and ADCH charges of **IM1-T$_1$**, **TS3-T$_1$** and **IM5-T$_1$** to clarify the cleavage mode of the C–F bond.

(Fig. 1a) with much higher stability can be detected when a mono-H-bonding donor, methanol, was used as the surrogate for water.

To understand the synergistic effects of the photo-activation and H-bonding on the initial defluorination, we compared the Laplacian bond order (LBO)[31] of the identical C–F bond in both **1a** and the first excited triplet state **1a-T$_1$**, the values of which are positively correlated with the bond energy of interest (Fig. 2b; the three-dimensional structures were generated using CYLview 20 [32]). In the excited state, one of the three C–F bonds is impaired, with LBO = 0.163 in **1a** and 0.111 in **1a-T$_1$**, respectively. Meanwhile, the water molecule also accelerates the C–F bond cleavage *via* H-bonding interactions with a decrease in the LBO in **IM1-T$_1$** (0.097). The hydrogen bond strength between HO–H and F atom in both **IM1** and **IM1-T$_1$** (triplet state) were estimated by the electron densities of the bond critical point (ρ_{BCP}) defined by AIM theory,[33] which were approximately −1.45 kcal mol^{-1} and −2.37 kcal mol^{-1}, respectively (Fig. 2b). These values are moderate in strength but essential in assisting the heterolysis of the C(sp^3)–F bond (LBO = 0.097 in **T$_1$**). Subsequently, the spin density isosurface and ADCH charge[34] for the key species (**IM1-T$_1$**, **TS3-T$_1$**, **IM5-T$_1$**) in the first defluorination process were also analysed (Fig. 2c, isosurface plots were generated using VMD 1.9.3 [35]) to evaluate the feasible electron transfer during the C–F bond cleavage. Consequently, the departing fluorine in **TS3-T$_1$** has a relatively low spin density (0.10) and a high negative charge (−0.46), indicating that the defluorination reaction is heterolysis rather than a radical process. This result is consistent with the experimental observation that radical quencher proceeds sluggishly in quenching the photo-DAFEx.

Evaluation of the substrate scopes

To meet the requirements for widespread application in both biochemistry and material science, it is necessary to explore the tolerance of photo-DAFEx toward substrates equipped with various chemical functionalities. Therefore, we commenced to synthesize a series of *m*-trifluoromethylaniline derivatives containing modular units (*e.g.*, –OH, –NHBoc, –CONH–), which were efficiently ligated with benzylamine in good yields (Table 1, **3aa–3ha**, 76–87%). Oxiranemethanol and terminal alkyne were also appended on the *m*-trifluoromethylaniline backbone for a sequential click strategy, which afforded 60–70% yields (**3ia–3ja**). A variety of functional units, including an NMR tag, biotin and PEG groups were examined, and all were tolerated well under the photo-DAFEx conditions to afford the products **3ka–3ma** (up to 82% yield). Afterwards, we also introduced natural products or drugs, including geraniol (**3na**), clofibric acid (**3oa**), sulfonamide (**3pa**), and cholic acid (**3qa**), in the photo-DAFEx chemistry, and obtained *N*-benzylbenzamide drug-conjugates in 62–90% yield. Generally, we were able to introduce diverse functionalities on the *m*-trifluoromethylaniline backbone without compromising the photo-defluorination in an aqueous environment.

We next evaluated the suitability of a series of nucleophiles in the photo-DAFEx. As shown in Table 1, primary/secondary

Table 1 Substrate scopes for the photo-DAFEx reaction[ab]

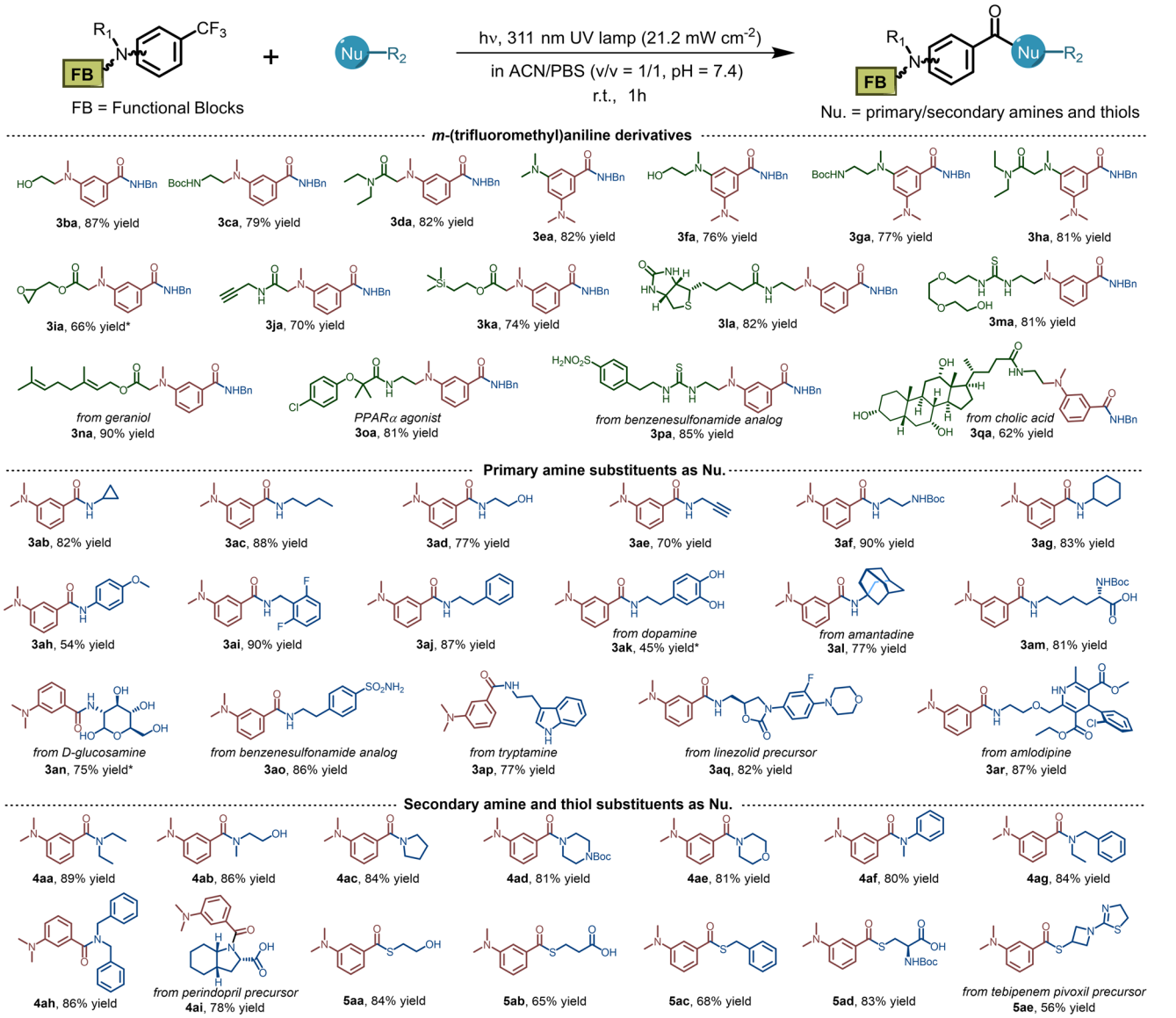

[a] Substrate scopes of the photo-DAFEx reaction. Reaction conditions: *m*-trifluoromethylaniline derivates (0.12 mmol) and nucleophiles (0.60 mmol) in 200 mL ACN/PBS ($v/v = 1/1$, pH = 7.4) were irradiated with a 311 nm lamp (21.2 mW cm^{-2}) for 1 h; isolated yields are given. [b] Reaction conditions: *m*-trifluoromethylaniline derivates (100 μM) and nucleophiles (500 μM) in 1.0 mL ACN/PBS ($v/v = 1/1$, pH = 7.4) were irradiated with a 311 nm lamp (5.9 mW cm^{-2}) for 60 s, and HPLC yields were determined *via* the calibration with external standard method.

amines and thiols could form a covalent linkage toward **1a** smoothly and generate amides (**3ab–4ai**) and thioesters (**5aa–5ae**), respectively. However, dopamine provided a relatively poor yield of **3ak** due to the photo-decomposition caused by the optical filtering effect of the pyrocatechol moiety. In comparison with *p*-anisidine (pKa_H = 5.3, 54% yield, **3ah**), pyridyl amines, such as 4-aminopyridine (pKa_H = −6.30) or aminopyrazine (pKa_H = −4.40), did not amidate with the benzoyl fluorides under physiological pH (= 7.4).[36] Remarkably, a diverse set of pharmaceutical building blocks and natural products are well tolerated as primary amine nucleophiles (**3am–3ar**). Representative aliphatic and aromatic secondary amines were further employed, most of which could be conjugated with benzoyl fluoride to furnish 78–91% yields of **4aa–4ai**, but pyrrole, indole and carbazole are unsuitable (Fig. S74, ESI†). Thioesters are important units in biosynthetic processes.[37] Finally, we examined the substrate scope for various thiols, including 2-mercaptoethanol, protected L-cysteine and 3-azetidinethiol (the intermediate of tebipenem). Pleasingly, all of the thiols could afford the thioester conjugate in up to 84% yields (**5aa–5ae**). Collectively, the photo-DAFEx exhibits good tolerance and high chemo-selectivity for a specific class of nucleophiles that is appropriate for drug target fishing.

Spectroscopic characterization and kinetics studies

When investigating the substrate scopes, significant fluorescence turn-on was observed during each photo-conjugation (Fig. 3). In the absence of nucleophiles, the initial photo-defluorination step (**1a–1h**) gives the corresponding benzoyl fluorides as poor fluorophores, and this step can be monitored by real-time tracking of the absorption spectra (Fig. S7, ESI†). To clarify the fluorogenic performance of the photo-DAFEx, fluorescence emission spectra were then recorded during the course of exposure to 311 nm irradiation in the presence of benzylamine. Reagents **1a–1h** were completely converted to the corresponding amides (**3aa–3ha**) within 60 s, accompanied by fluorogenic turn-on in a time-resolved manner (Fig. 3a, b and S8, ESI†). The turn-on ratios were determined to be 27-fold and 65-fold for **3aa** and **3ca** at the maximum emission wavelengths, respectively. Moreover, **3aa–3ca** displayed much stronger fluorescence intensity than **3ea–3ha** with two *N*,*N*-dimethylamine substitutions (Fig. S8, ESI†). Histidine, lysine, and cysteine were also subjected to the fluorogenic assessment in the photo-DAFEx, and only *N*-Boc-L-lysine appeared to have the turn-on character (up to 53-fold, Fig. S9 and 10, ESI†).

Taking advantage of this fluorogenic feature, the second-order rate constant for the conjugation step between benzoyl fluoride and benzylamine could be facilely determined to be ~145 M^{-1} s^{-1} (Fig. 3c), which is almost comparable to that of tetrazines-BCN IEDDA[38] and faster than that of CuAAC.[4] Fluorescence spectra of **3aa** in various solvents were further measured, and the intensity decreased sharply along with bathochromic shift of the emission band when the dielectric constant (ε) of the solvent system was increased, except in the case of DMSO (Fig. 3d). The absolute fluorescence quantum

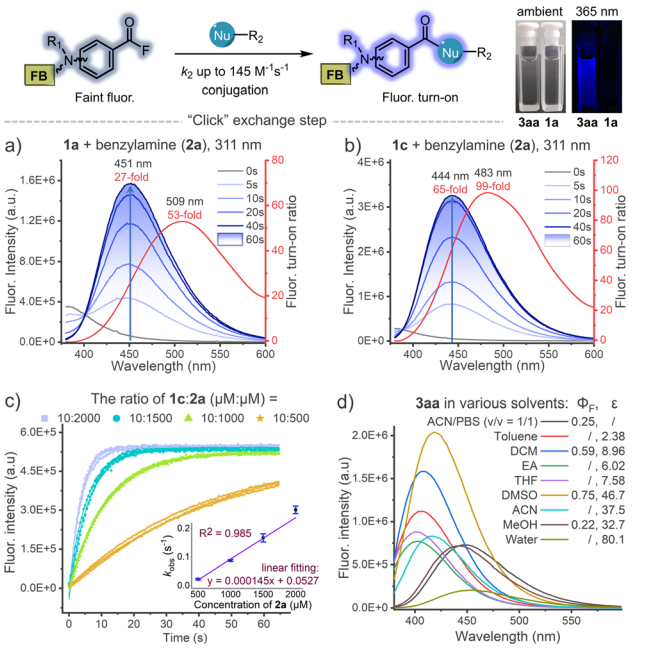

Fig. 3 Dynamic tracking of fluorescence turn-on during the photo-DAFEx reaction between (a) **1a** (100 μM) or (b) **1c** (100 μM) and benzylamine (**2a**, 500 μM) in ACN/PBS (v/v = 1/1, pH = 7.4) under 311 nm irradiation (5.9 mW cm^{-2}), the turn-on ratio was plotted along with the emission wavelength (red curve); for more details, see Table S3, ESI†. (c) Kinetic study of the acyl exchange step between **1c** and **2a** in ACN/PBS (v/v = 1/1, pH = 7.4) to obtain the second-order reaction rate; λ_{ex} = 345 nm, λ_{em} = 445 nm. (d) Fluorescence emission spectra of the isolated **3aa** (50 μM) in various solvents with quantum yield (Φ_F) and dielectric constant (ε) of the solvent denoted; λ_{ex} = 338 nm.

yields (Φ_F) were also then determined, and showed a consistent trend with the spectral measurements, in which **3aa** in DMSO showed the highest value of up to Φ_F = 0.75 (Table S3, ESI†).

Photo-controlled peptide cyclization and decoration

Encouraged by the high efficiency and controllability, we began to unravel the potential of photo-DAFEx in polypeptide conjugation. Based on HPLC-MS screening of free amino acids (Table S6 and Fig. S75–76, ESI†), only L-histidine, L-cysteine and L-lysine are readily targeted by reagent **5a** in the photo-DAFEx, implying that about 8.83% of natural residues are available for profiling (Fig. 4a).[39] To reveal the residual preference, competitive tests were further performed, which resulted in a ligation product ratio of 52 : 17 : 26 (Fig. 4b), respectively.

The rigid conformation and topology of cyclic peptides dominate their unique functions and resistance toward enzymatic proteolysis, which has aroused considerable attention in bio-macromolecular drug design.[40] To be able to control the cyclization of the unprotected peptide *via* the photo-DAFEx, we firstly joined the photo-DAFEx warhead onto a cysteine residue of the linear peptides *via* the α-halocarbonyl reagents **1r** and **1s** (Fig. S77–84, ESI†). Then, 311 nm irradiation could be applied to induce a temporally

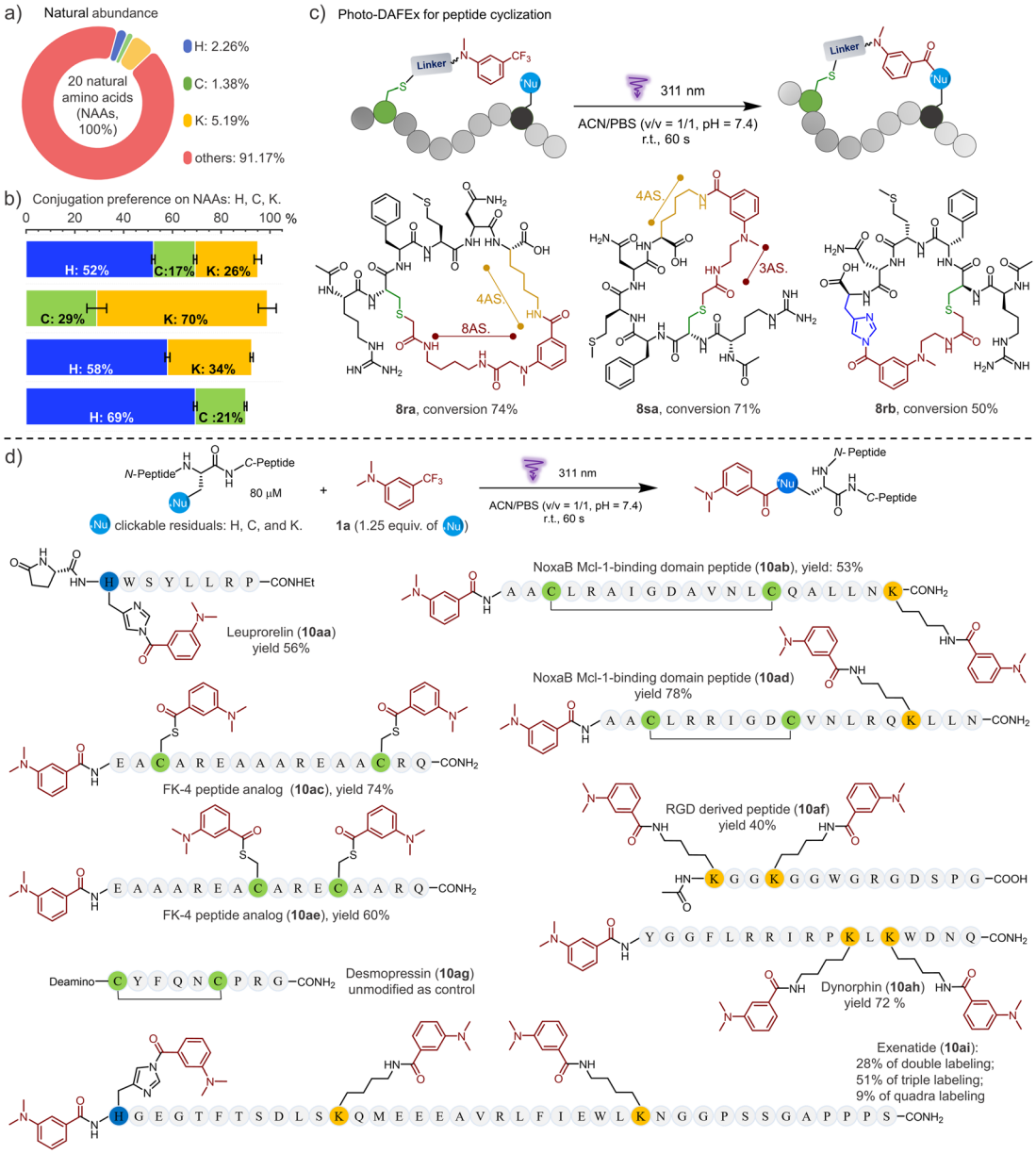

Fig. 4 Photo-DAFEx for controllable peptide cyclization and conjugation. (a) Natural abundance of each photo-clickable NAA available on proteins for the photo-DAFEx. (b) Preference of the photo-DAFEx for histidine (blue), cysteine (lime) and lysine (yellow) residues using **5a**, analysed *via* an HPLC competition test with **1a** (100 μM) and each NAA (500 μM) in 1.0 mL of ACN/PBS (*v*/*v* = 1/1, pH = 7.4); 311 nm lamp irradiation (5.9 mW cm^{-2}) for 60 s. (c) Photo-DAFEx for peptide cyclization toward lysine and histidine residues in accessible proximity. Conditions: 100 μM peptide, 311 nm lamp irradiation (5.9 mW cm^{-2}) for 60 s, for more details, see ESI†; (d) peptide conjugation *via* photo-DAFEx on L-histidine, L-lysine, free L-cysteine residues and *N*-terminal amines. Reaction conditions: peptide (80 μM) and **1a** (1.25 equiv. for all photo-clickable NAAs residues at 100–400 μM) in ACN/PBS (*v*/*v* = 1/1, pH = 7.4) were treated with 311 nm lamp irradiation (5.9 mW cm^{-2}) for 60–90 s; HPLC yields were determined using an external standard. AS. = atoms.

controlled cyclization toward available histidine/lysine residues within an acceptable proximity (Fig. 4c and S76–83, ESI†). Owing to the side-chain flexibility and stability of the resulting amide, the L-lysine residue as the cyclization juncture exhibited excellent ring-forming capability in comparison with L-histidine. However L-histidine, a reactive and reversible cyclization juncture in photo-DAFEx, is worthy of in-depth exploration for peptide medicines.

Next, the photo-DAFEx toward various functional peptides containing multiple nucleophilic residues was conducted to assess the universality for multi-decoration (Fig. 4d). Leuprorelin (**9a**) was first chosen to test the reactivity toward histidine residues on peptides, which afforded a conjugate in 56% yield (**10aa**). The resulting *N*-acyl imidazole as a moderate electrophile has great potential to be applied in sequential bioconjugations and enzyme activation.[41,42] Disulfide bonds play

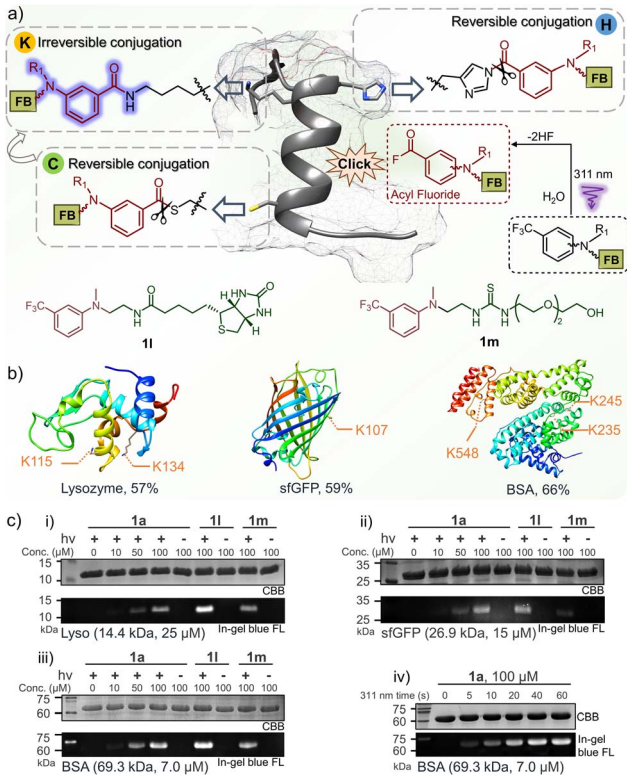

Fig. 5 Fluorogenic and temporally controlled protein decorations *via* the photo-DAFEx reaction. (a) Characteristics of protein labeling toward lysine, histidine or cysteine residues, and the structure of **1l** and **1m**. (b) Site precedence of the photo-labeling on lysozyme, sfGFP and BSA, which was determined by LC-MS/MS analysis (Fig. S12–16, ESI†). The photo-labeling conversions were determined by deconvoluting the charge ladder of ion counting of the intact proteins in LC-MS spectra; for more details see Fig. S17, ESI†. (c) Fluorogenic protein decoration *via* photo-DAFEx (i–iii) visualized by in-gel fluorescence imaging and (iv) a time-course of light irradiation (5.9 mW cm^{-2}) for 0–60 s. Reaction conditions: proteins (4.0 mg mL^{-1}) and *m*-trifluoromethylaniline reagents in PBS were treated with/without 311 nm irradiation, and then resolved by SDS-PAGE for imaging. CBB = coomassie brilliant blue; FL = fluorescence channel.

a critical role in governing the conformation of proteins, and thus being inert towards them is necessary for a successful photo-bioconjugation strategy. Fortunately, no rupture of the disulfide bonds was observed after treating desmopressin (**9g**) with **1a** under 311 nm irradiation (Fig. S91, ESI†). After the same treatments of the disulfide-bond-cyclized NoxaB protein fragments (**9b**/**9d**), no quadra-labelled products were detected in HPLC-MS, but double-decoration of both the *N*-terminal and the lysine residue (**10ab** and **10ad**) were identified. In contrast, when there are two free cysteines available on FK-4 peptide analogues (**9c** and **9e**), dual photo-thioesterification was allowed, with 74% and 60% yields, respectively. Moreover, RGD peptide analogue (**9f**) and Dynorphin (**9h**) with double lysine residues also showed good multi-ligation reactivities. For Exenatide (**9i**) with a long chain, a variety of multi-labelled products were detected, among which a tri-modified Exenatide (**10ai**) was mainly distributed in 51% yield (Fig. S93, ESI†).

Fluorogenic protein decoration

To understand the conjugation efficiency of photo-DAFEx on proteins, wild-type lysozyme, super-fold green fluorescent protein (sfGFP) and bovine serum albumin (BSA) were photo-labelled by using **1a** (Fig. 5a). The decoration efficiency was found to be 57%, 59%, and 66%, respectively (Fig. 5b and S17, ESI†). The photo-labeling conversion would be improved with increasing the dosage of **1a**, but at the cost of site-specificity (Fig. S18, ESI†). The site precedence of the labeling was then analysed using LC-MS/MS splicing, and we found the solvent exposed lysine sites, namely, the K115 and K134 sites on lysozyme, K107 on sfGFP, and K235, K245 and K548 on BSA, were labelled (Fig. 5b and S12–16, ESI†), while other lysine residues cannot be accessed because of inappropriate proximity. Only lysine decorations could be identified by LC-MS/MS, rather than histidine or cysteine decoration, which is attributed to the reversible nature of the latter two types of conjugates and their rare occupancy, as well as the inactive disulfide form.[41–43] In-gel fluorescence analysis is an intuitive way to demonstrate the fluorogenic decoration of proteins. Therefore, a concentration gradient of **1a** (0–100 μM) was used for a temporally controlled modification toward the three proteins *via* photo-irradiation. As a result, clear blue fluorescence bands can be observed at the level of 50 μM **1a**, while no signal can be detected in the absence of 311 nm irradiation (Fig. 5c(i)). Similarly, **1l** with a biotin tag and **1m** with a PEG tail were also successfully photo-conjugated on the three proteins with fluorescence turn-on (Fig. 5c(i–iii)). Moreover, the fluorogenic labeling of BSA occurred in a time-dependent manner, suggesting a satisfactory temporal controllability (Fig. 5c(iv)). However, no background protein decoration was observed even after 2 h incubation in the dark (Fig. S19, ESI†). Therefore, the fluorogenic photo-DEFAx of proteins could greatly facilitate visualization of the photo-conjugation process in complex biological systems without the need for washing or extra staining procedures.

Photo-affinity labeling (PAL) for hCA-II

Drug-target interactions play an essential role in adjusting the functions of the targets for rescuing intrinsic cell activities. Hence, understanding of dynamic drug-target interaction networks *via* covalent capture offers great opportunities for therapeutics and drug discovery, especially for disease-related enzymes.[19] The PAL strategy allows covalent binding to the targets with temporal control, thus enabling the identification of new drug targets and related molecular interactions.[44] To demonstrate the PAL capability of the photo-DAFEx in cross-linking with lysine, we chose human carbonic anhydrase II (hCA-II) as the target owing to its availability, stability and structural clarity.[45] hCA-II catalyses the reversible hydration of carbon dioxide, and it can be competitively inhibited by aryl sulfonamides, such as acetazolamide (AZA, K_i = 12.1 nM, Fig. S22, ESI†).[46,47] Accordingly, photo-DAFEx-based PAL probes were designed and constructed *via* the fusion of *m*-trifluoromethylaniline into aryl sulfonamide (**10a–10f**, Fig. 6a and Table S7, ESI†). Before PAL, the efficacy of these probes toward hCA-II was confirmed to be IC_{50} = 0.95 and 1.12 μM for **10a** and

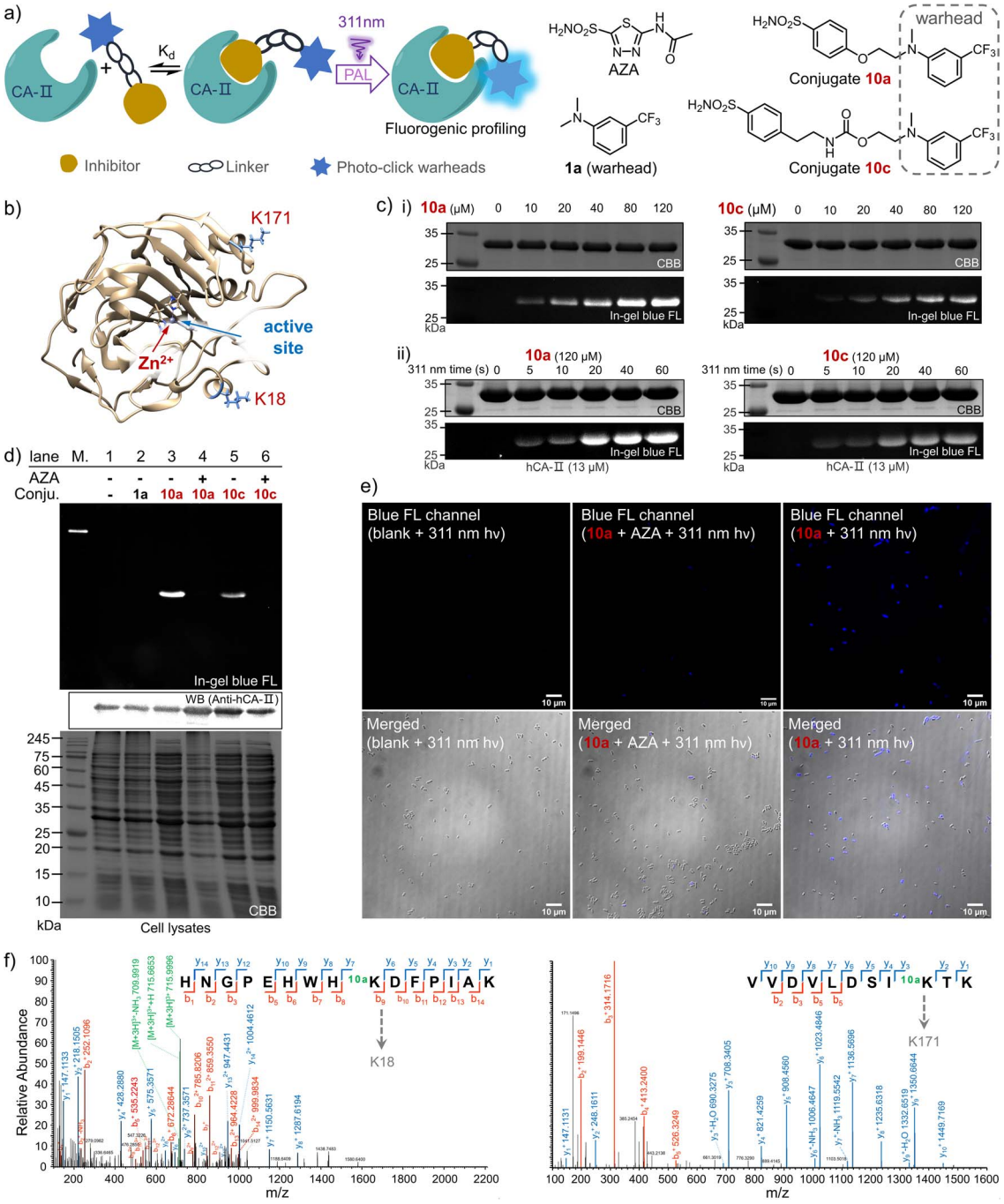

Fig. 6 Photo-affinity labeling of hCA-II by *m*-trifluoromethylaniline-drug probes through the fluorogenic photo-DAFEx. (a) Schematic illustration of the PAL and the structure of the probes, commercial inhibitor and control reagent (**1a**). (b) Crystal structure of hCA-II showing the Zn^{2+} in the active site and the photo-labelled lysine residues. (c) In-gel fluorescence imaging of the SDS-PAGE for resolving the hCA-II (13 μM) after photo-labeling by probes **10a**/**10c** with irradiation *via* a 311 nm lamp (5.9 mW cm^{-2}): (i) concentration gradient after 60 s irradiation and (ii) irradiation time-course. (d) Fluorogenic photo-labeling of hCA-II in *E. coli* lysate *via* the photo-DAFEx by probe **10a**/**10c** (20 μM) in the presence/absence of the competitive inhibitor AZA (1.0 mM) with irradiation *via* a 311 nm lamp (5.9 mW cm^{-2}) for 30 s, with **1a** as a negative control. (e) Fluorescence microscopic imaging of the *E. coli* cells (BL21(DE3)) overexpressing the hCA-II after PAL with probe **10a** (5 μM) under 311 nm irradiation (5.9 mW cm^{-2}) for 60 s. Scale bar = 10 μm; $\lambda_{ex}/\lambda_{em}$ = 365/420–470 nm, 100× oil-immersion objective. (f) LC-MS/MS analysis of the peptide fragment from trypsin digested hCA-II after photo-labeling by probe **10a**.

10c (Fig. S22, ESI†), respectively, which is slightly weaker than that of commercial AZA (IC_{50} = 0.70 μM).[46] Then, probe concentration gradients (0–120 μM) and an irradiation time-course (0–60 s) were evaluated in the photo-DAFEx toward hCA-II (Fig. 6c). In-gel fluorescence analysis clarified that an approximately 10 μM dosage of probes **10a** and **10c** is the

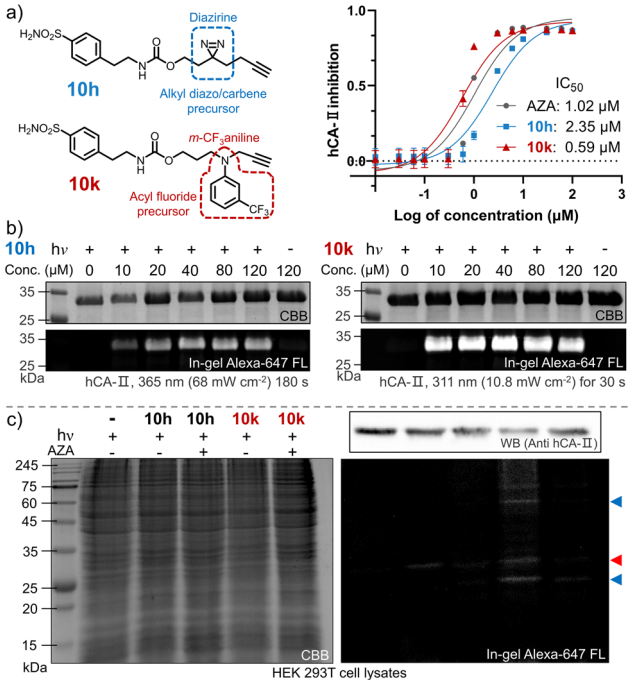

Fig. 7 Photo-affinity labeling of hCA-II *via* an alkyl diazirine probe *vs.* *m*-trifluoromethylaniline-inhibitor conjugate. (a) Structural illustration of **10h** *vs.* **10k**, and plot of the enzymatic activity of hCA-II to catalyse hydrolysis of *p*-nitrophenyl acetate *vs.* inhibitor concentration. Error bars indicate SD, $n = 3$. (b) In-gel fluorescence imaging of SDS-PAGE of the resolved hCA-II (13 μM) after photo-labeling by probes **10h** (left) and **10k** (right). (c) SDS-PAGE analysis of endogenous proteins after photo-labeling by **10h** *vs.* **10k** (5.0 μM) in the presence/absence of AZA (25 μM) in living HEK 293T cells. Note: hCA-II is marked by a red triangle; other photo-labelled proteins are marked by blue triangles. Fluorophore attachment was realized *via* CuAAc with an azide-Alexa-647 conjugate.

minimum for *in vitro* studies (Fig. 6c(i)), and obvious fluorescence bands appeared after 20 s of irradiation in the time-course tracking (Fig. 6c(ii)). Thus, *in vitro* PAL in protein mixtures containing lysozyme, BSA and recombinant hCA-II or in cell lysates were further tested to understand the ligand-directed target specificity, and were also visualized using in-gel fluorescence (Fig. S20, ESI†). In bacterial lysates, only the lanes treated with either **10a** or **10c** displayed strong fluorescence bands with the correct size of hCA-II after photo-DAFEx reaction, confirming their strong affinity toward hCA-II (Fig. S21, ESI†).

To verify the specific binding of **10a** and **10c** to the active pocket of hCA-II, a set of control experiments was also examined (Fig. 6d). First, no fluorescent band in lane 2 was observed when **1a** without the sulfonamide drug moiety was used as a negative control, while strong fluorescence signals correlated to hCA-II were visualized in lanes 3 (**10a**) and 5 (**10c**), suggesting that their aryl sulfonamide moieties dominate the binding toward hCA-II in bacterial lysates. When the PAL probes competed against a 50-fold excess of AZA, the fluorescence bands were both quenched (lanes 4 and 6). Therefore, it is clear that the PAL probes bind competitively at the same active site of hCA-II as AZA, where the zinc(II)-histidine complex is located (Fig. 6b).[47]

In addition, a fluorescent western blot analysis confirmed that the hCA-II was evenly loaded among all lanes (Fig. 6d). Furthermore, the deconvoluted mass spectra also indicated that each molar equivalent of hCA-II can be crosslinked with only one molar equivalent of the probe (Fig. S23, ESI†). To determine the possible photo-labeling residues for **10a**, the crosslinked hCA-II was further subjected to LC-MS/MS analysis (Fig. 6f), and the spliced peptide fragment revealed that K18 and K171 are two preferred sites for photo-crosslinking. Both are located near the entrance to the binding pocket of hCA-II (Fig. 6b and Tables S4 and 5, ESI†). Benefiting from the fluorogenic nature of photo-DAFEx, bright blue fluorescence signals could be visualized in living *E. coli* cells after the PAL toward hCA-II surrounded by endogenous proteins (Fig. 6e). However, the fluorescence was still diminished in the presence of the competitive AZA. Noticeably, variable expression levels of hCA-II lead to uneven turn-on signals among *E. coli* cells, which stems from the randomness of transcription and translation in each cell.[48] Taken altogether, the PAL probe **10a** is capable of fishing for the ligand-directed targets in both *in vitro* and *in vivo* studies with the added benefit of fluorogenic imaging, which could inspire utilization of the photo-DAFEx chemistry in pharmacological research.

PAL of endogenous hCA-II in living cells

The ultimate goal of PAL is to capture endogenous proteins with high affinity in living cells under photo-control. Herein, we evaluated the potential of the photo-DAFEx chemistry in PAL profiling *via* side-by-side comparisons with diazirine photolysis in HEK-293T cells, which express hCA-II endogenously (Fig. S24, ESI†). The two types of PAL probes were first synthesized (Fig. 7a). **10g** is a well-known alkyl-diazirine-based photo-affinity probe with a terminal alkyne for CuAAC fluorescence imaging;[49] while **10k** is a structurally similar probe but based on the photo-DAFEx warhead. In the enzymatic inhibition assay for hCA-II, both of the probes could target the active pocket, showing high inhibition efficiency ($IC_{50} = 2.35$ μM and 0.59 μM for **10h** and **10k**, respectively) in comparison with commercial AZA ($IC_{50} = 1.02$ μM). After CuAAC to the PAL-tagged terminal alkyne on hCA-II *in vitro via* azide-Alexa-647 (Fig. S25, ESI†), in-gel fluorescence imaging indicated significant brighter bands for hCA-II with the probe **10k** even at 10 μM, clarifying that **10k** possesses higher photo-labeling efficiency than **10h** (Fig. 7b). In-gel fluorescence comparison for hCA-II in bacterial lysates also exhibited similar results, in which the photo-DAFEx (**10k**) displayed much stronger fluorescence band over the diazirine photolysis (**10h**) (Fig. S25, ESI†).

We next examined whether the *in vitro* efficiency differences between alkyl diazirine photolysis and photo-DAFEx corresponded to those for endogenous hCA-II in living mammalian cells. After incubating the two probes at 5.0 μM in HEK-293T cells for 2 h, the cells were exposed to irradiation, lysed, and clicked with azide-Alexa-647 for visualization using SDS-PAGE. The fluorescence bands (Fig. 7c, marked with red triangles) corresponding to hCA-II were then observed for the cells treated with the two individual probes and irradiation,

and suggested good reactivity of the photo-DAFEx chemistry for drug-target profiling. Western blot (upper right panel, Fig. 7c) analysis confirmed that hCA-II was evenly expressed among the groups of cells, matching with the molecular weight of the fluorescent bands. Side-by-side in-gel comparison between the probes **10h** and **10k** (lower right panel, Fig. 7c) showed that the alkyl-diazirine-based PAL exhibited almost a single hCA-II band without potential off-target bands, while the photo-DAFEx displayed multiple bands. Because the acyl fluoride intermediate generated by the photo-defluorination of **10k** is much more stable ($t_{1/2}$ = 13.7 h) than the alkyl diazo intermediates ($t_{1/2} \approx$ 70 s)[50] or the alkyl carbene intermediates ($t_{1/2} \approx$ 2 ns),[24] more relevant protein targets interacting with the **10k** probe with inferior affinity were able to be captured. Thus, the multiple fluorescence bands (Fig. 7c, marked with blue triangles) could possibly be attributed to secondary protein interactions with **10k** in mammalian cells, which can be mostly blocked by the AZA inhibitor. The long half-life of the photo-generated intermediate might result in an increased labeling radius from the drug binding site, depending on flexibility of the linker,[24] which might result in off-target ligation. In contrast, a short-lived intermediate is excellent for designing PAL probes for drug profiling with fast binding kinetics and high spatial accuracy, but also leads to high sensitivity to the microenvironment and proximity. A long-lived intermediate with a flexible linker has sufficient degrees of freedom to rotate and stretch, and subsequently to capture inferior-affinity targets, which may find use in drug/target discovery because weakly interacting targets sometimes are cofactors for drug efficacy.[50] Nevertheless, these results convincingly demonstrated the photo-DAFEx chemistry could be applied in PAL for drug profiling, which expands the arsenal for target verification, especially in combination with the short-lived but reactive diazo/carbene intermediates.

Conclusions

A photo-DAFEx system was developed for convenient controllable photo-conjugation toward primary/secondary amines and thiols under mild conditions. *m*-Trifluoromethylaniline serving as a photo-crosslinking module produces a relatively stable and easy-to-handle intermediate, benzoyl fluoride, *via* water-mediated photo-defluorination. Theoretical calculations and experimental evidence revealed that the $PhF_2C(sp^3)$–F bond is weakened in the excited triplet state by water molecules. Subsequent amidation of benzoyl fluoride shows a fluorogenic feature, which allows visualization of the covalent bond formation *in situ*. Based on these characteristics, exploitation of the photo-DAFEx in small-molecule conjugation, peptide cyclization, direct peptide/protein modification was successful. This strategy has also been expanded in PAL for fishing for drug targets in living mammalian cells. Given the unique nucleophile preference on native residues, the advancement of photo-DAFEx holds great potential for photo-defluorination synthesis, pharmacological research and 3D photo-printing of biomaterials.

Data availability

Additional figures as described in the main text, all experimental procedures, synthetic procedures, copies of spectral data for the compounds, data processing, and computational details are available in the ESI.†

Author contributions

L. D., Z. S., and Z. Y. initiated the idea, designed the experiments and wrote the manuscript. L. D. synthesized the main compounds and conducted all of the experiments. C. Z., Z. S., and C. H. carried out the theoretical calculations. B. l., Z. Z., J. F., T. L., and X. Z. helped with compound synthesis and *in vitro* experiments. All authors contributed to the manuscript.

Conflicts of interest

There are no conflicts to declare.

Acknowledgements

Financial support was provided by the National Natural Science Foundation of China (22001181 and 22077090), the Fundamental Research Funds for the Central Universities (20826041D4117) and the Institutional Research Fund from Sichuan University (2020SCUNL105). We also express our appreciation to Dr Lunzhi Dai at State Key Laboratory of Biotherapy and Cancer Center, West China Hospital, Sichuan University, for help with the LC-MS/MS analysis. We also thank the Xiaoming Feng laboratory (Sichuan University) for access to equipment.

Notes and references

1 J. Dong, K. Krasnova, M. G. Finn and K. B. Sharpless, *Angew. Chem., Int. Ed.*, 2014, **53**, 9430.
2 G. J. Brighty, R. C. Botham, S. Li, L. Nelson, D. E. Mortenson, G. Li, C. Morisseau, H. Wang, B. D. Hammock, K. B. Sharpless and J. W. Kelly, *Nat. Chem.*, 2020, **12**, 906.
3 Q. Li, Q. Chen, P. C. Klauser, M. Li, F. Zheng, N. Wang, X. Li, Q. Zhang, X. Fu, Q. Wang, Y. Xu and L. Wang, *Cell*, 2020, **182**, 85.
4 (*a*) T. Tamura and I. Hamachi, *J. Am. Chem. Soc.*, 2018, **141**, 2782; (*b*) N. Wang, B. Yang, C. Fu, H. Zhu, F. Zheng, T. Kobayashi, J. Liu, S. Li, C. Ma, P. G. Wang, Q. Wang and L. Wang, *J. Am. Chem. Soc.*, 2018, **140**, 4995.
5 D. Medina-Cleghorn, L. A. Bateman, B. Ford, A. Heslin, K. J. Fisher, E. D. Dalvie and D. K. Nomura, *Chem. Biol.*, 2015, **22**, 1394.
6 G. S. Kumar and Q. Lin, *Chem. Rev.*, 2020, **121**, 6991.
7 B. D. Fairbanks, L. J. Macdougall, S. Mavila, J. Sinha, B. E. Kirkpatrick, K. S. Anseth and C. N. Bowman, *Chem. Rev.*, 2021, **121**, 6915.
8 Q. Xiong, T. Zheng, X. Shen, B. Li, J. Fu, X. Zhao, C. Wang and Z. Yu, *Chem. Sci.*, 2022, **13**, 3571.
9 A. A. Poloukhtine, N. E. Mbua, M. A. Wolfert, G. J. Boons and V. V. Popik, *J. Am. Chem. Soc.*, 2009, **131**, 15769.

10 G. S. Kumar, S. Racioppi, E. Zurek and Q. Lin, *J. Am. Chem. Soc.*, 2022, **144**, 57.
11 L. Zhang, X. Zhang, Z. Yao, S. Jiang, J. Deng, B. Li and Z. Yu, *J. Am. Chem. Soc.*, 2018, **140**, 7390.
12 S. Arumugam and V. V. Popik, *J. Am. Chem. Soc.*, 2011, **133**, 5573.
13 S. V. Mayer, A. Murnauer, M. von Wrisberg, M. Jokisch and K. Lang, *Angew. Chem., Int. Ed.*, 2019, **58**, 15876.
14 C. E. Hoyle and C. N. Bowman, *Angew. Chem., Int. Ed.*, 2010, **49**, 1540.
15 S. S. Zalesskiy, N. S. Shlapakov and V. P. Ananikov, *Chem. Sci.*, 2016, **7**, 6740.
16 J. Li, H. Kong, L. Huang, B. Cheng, K. Qin, M. Zheng, Z. Yan and Y. Zhang, *J. Am. Chem. Soc.*, 2018, **140**, 14542.
17 Z. Li, L. Qian, L. Li, J. C. Bernhammer, H. V. Huynh, J. S. Lee and S. Q. Yao, *Angew. Chem., Int. Ed.*, 2016, **55**, 2002.
18 W. Hu, Y. Yuan, C. H. Wang, H. T. Tian, A. D. Guo, H. J. Nie, H. Hu, M. Tan, Z. Tang and X. H. Chen, *Chem*, 2019, **5**, 2955.
19 H. Fang, B. Peng, S. Y. Ong, Q. Wu, L. Li and S. Q. Yao, *Chem. Sci.*, 2021, **12**, 8288.
20 S. Y. Dai and D. Yang, *J. Am. Chem. Soc.*, 2020, **142**, 17156.
21 K. Cheng, J. S. Lee, P. Hao, S. Q. Yao, K. Ding and Z. Li, *Angew. Chem., Int. Ed.*, 2017, **56**, 15044.
22 A. C. S. Page, S. O. Scholz, K. N. Keenan, J. N. Spradlin, B. P. Belcher, S. M. Brittain, J. A. Tallarico, J. M. Mckenna, M. Schirle, D. K. Nomura and F. D. Toste, *Chem. Sci.*, 2022, **13**, 3851.
23 A. D. Guo, D. Wei, H. J. Nie, H. Hu, C. Peng, S. T. Li, K. N. Yan, B. S. Zhou, L. Feng, C. Fang, M. Tan, R. Huang and X. H. Chen, *Nat. Commun.*, 2020, **11**, 5472.
24 J. V. Oakley, B. F. Buksh, D. F. Fernández, D. G. Oblinsky, C. P. Seath, J. B. Geri, G. D. Scholes and D. W. C. MacMillan, *Proc. Natl. Acad. Sci. U. S. A.*, 2022, **119**, e2203027119.
25 S. Rafqah and M. Sarakha, *J. Photochem. Photobiol., A*, 2016, **316**, 1.
26 T. Stahl, H. F. T. Klare and M. Oestreich, *ACS Catal.*, 2013, **3**, 1578.
27 Y. Ogiwara and N. Sakai, *Angew. Chem., Int. Ed.*, 2020, **59**, 574.
28 V. Glembockyte, R. Lincoln and G. Cosa, *J. Am. Chem. Soc.*, 2015, **137**, 1116.
29 T. Lu and Q. Chen, *Comput. Theor. Chem.*, 2021, **1200**, 113249.
30 T. Lu and F. Chen, *J. Comput. Chem.*, 2012, **33**, 580.
31 T. Lu and F. Chen, *J. Phys. Chem. A*, 2013, **117**, 3100.
32 C. Y. Legault, *CYLview20*, Université de Sherbrooke, 2020, **http://www.cylview.org**.
33 S. Emamian, T. Lu, H. Kruse and H. Emamian, *J. Comput. Chem.*, 2019, **40**, 2868.
34 T. Lu and F. Chen, *J. Theor. Comput. Chem.*, 2012, **11**, 163.
35 W. Humphrey, A. Dalke and K. Schulten, *J. Mol. Graphics*, 1996, **14**, 33.
36 E. K. Woodman, J. G. K. Chaffey, P. A. Hopes, D. R. J. Hose and J. P. Gilday, *Org. Process Res. Dev.*, 2014, **13**, 106.
37 F. Seidi, R. Jenjob and D. Crespy, *Chem. Rev.*, 2018, **118**, 3965.
38 W. Mao, J. Tang, L. Dai, X. He, J. Li, L. Cai, P. Liao, R. Jiang, J. Zhou and H. Wu, *Angew. Chem., Int. Ed.*, 2021, **60**, 2393.
39 L. P. Kozlowski, *Nucleic Acids Res.*, 2017, **45**, D1112.
40 H. Y. Chow, Y. Zhang, E. Matheson and X. Li, *Chem. Rev.*, 2019, **119**, 9971.
41 A. W. Dodds, X. D. Ren, A. C. Willis and S. K. A. Law, *Nature*, 1996, **379**, 177.
42 T. Mino, S. Sakamoto and I. Hamachi, *Biosci., Biotechnol., Biochem.*, 2021, **85**, 53.
43 J. Kim, B. X. Li, Y. C. Huang, J. X. Qiao and D. W. C. Macmillan, *J. Am. Chem. Soc.*, 2020, **142**, 21260.
44 E. Smith and I. Collins, *Future Med. Chem.*, 2015, **7**, 159.
45 K. Teruya, K. F. Tonissen and S. A. Poulsen, *MedChemComm*, 2016, **7**, 2045.
46 A. A. Barrese, C. Genis, S. Z. Fisher, J. N. Orwenyo, M. T. Kumara, S. K. Dutta, E. Phillips, J. J. Kiddle, C. Tu, D. N. Silverman, L. Govindasamy, M. Agbandje-McKenna, R. McKenna and B. C. Tripp, *Biochemistry*, 2008, **47**, 3174.
47 A. D. Fiore, E. Truppo, C. T. Supuran, V. Alterio, N. Dathan, F. Bootorabi, S. Parkkila, S. M. Monti and G. De Simone, *Bioorg. Med. Chem. Lett.*, 2010, **20**, 5023.
48 M. B. Elowitz, A. J. Levine, E. D. Siggia and P. S. Swain, *Science*, 2002, **297**, 1183.
49 Z. Li, P. Hao, L. Li, C. Y. J. Tan, X. Cheng, G. Y. J. Chen, S. K. Sze, H. M. Shen and S. Q. Yao, *Angew. Chem., Int. Ed.*, 2013, **52**, 8551.
50 B. Procacci, S. S. Roy, P. Norcott, N. Turner and S. B. Duckett, *J. Am. Chem. Soc.*, 2018, **140**, 16855.